

On-surface potential and radial electric field variations in electron root stellarator plasmas

J. M. García-Regaña¹, T. Estrada¹, I. Calvo¹, J. L. Velasco¹, J. A. Alonso¹, D. Carralero¹, R. Kleiber², M. Landreman³, A. Mollén², E. Sánchez¹, C. Slaby², TJ-II Team and W7-X Team

¹ Laboratorio Nacional de Fusión CIEMAT, Av. Complutense 40, 28040 Madrid, Spain

² Max-Planck-Institut für Plasmaphysik, Wendelsteinstr. 1, 17491 Greifswald, Germany

³ Institute for Research in Electronics and Applied Physics, University of Maryland, College Park, Maryland 20742, USA

E-mail: jose.regana@ciemat.es

Abstract. In the present work we report recent radial electric field measurements carried out with the Doppler reflectometry system in the TJ-II stellarator. The study focuses on the fact that, under some conditions, the radial electric field measured at different points over the same flux surface shows significantly different values. A numerical analysis is carried out considering the contribution arising from the radial dependence of Φ_1 as a possible correction term to the total radial electric field. Here Φ_1 is the neoclassical electrostatic potential variation over the surface. The comparison shows good agreement in some aspects, like the conditions under which this correction is large (electron-root conditions) or negligible (ion-root conditions). But it disagrees in others like the sign of the correction. The results are discussed together with the underlying reasons of this partial disagreement.

In addition, motivated by the recent installation of the dual Doppler reflectometry system in Wendelstein 7-X (W7-X), Φ_1 estimations for W7-X are revisited considering Core-Electron-Root-Plasma (CERC) plasmas from its first experimental campaign. The simulations show larger values of Φ_1 under electron-root conditions than under ion root. The contribution from the kinetic electron response is shown to become important at some radii. All this results in a potential variation size in W7-X noticeably larger than estimated in our previous [1] for other plasma parameters and another configuration.

1. Introduction

The radial electric field is one of the physical quantities with significant prominence in stellarator transport physics problems. In particular, for the radial transport of impurities and their accumulation, its role becomes more important as the charge state of the impurity increases. In stellarators, the explanation for this is framed by the standard neoclassical formalism. There, one can express the flux-surfaced-averaged fluxes as a

linear combination of thermodynamic forces and the so-called thermal transport matrix coefficients L_{ij}^a :

$$\frac{\langle \mathbf{\Gamma}_a \cdot \nabla r \rangle}{n_a} = -L_{11}^a \left(\frac{n'_a}{n_a} - \frac{Z_a e E_r}{T_a} + \frac{L_{12}^a}{L_{11}^a} \frac{T'_a}{T_a} \right), \quad (1)$$

with a the species index, n_a the density, T_a the temperature, Z_a the charge state, e is the proton charge, $\mathbf{\Gamma}_a$ the particle flux density and $\langle \dots \rangle$ the flux surface average operator. In the present work r is a flux surface label with the character of an effective radial coordinate such that the volume enclosed by a flux surface is $V = 2\pi^2 R_0 r^2$, and R_0 is the major radius of the stellarator. The prime $'$ denotes differentiation with respect to r . The radial electric field vector is $\mathbf{E}_r = E_r \nabla r$ with $E_r = -\Phi'_0$ and $\Phi_0 = \Phi_0(r)$ the part of the electrostatic potential constant on the flux surface. An important well-known difference between particle transport in stellarators respect to that in (axi-symmetric) tokamaks is that the particle transport of the different species does not obey ambipolarity at any E_r . In other words, the total radial flux-surface-averaged current does not vanish and quasi-neutrality is not preserved along the radial direction. Then, the radial electric field in stellarators is determined by imposing this ambipolarity condition, that reads, see e.g. [2],

$$\sum_a Z_a e \langle \mathbf{\Gamma}_a \cdot \nabla r \rangle = 0. \quad (2)$$

Despite the apparently explicit linear dependence of the fluxes on E_r , see eq. (1), the role that the radial electric field plays on the confinement of the trapped particle orbits in the long-mean-free-path regimes, makes the matrix transport coefficients depend also on E_r . This leads the ambipolarity condition to become a non-linear equation with multiple roots [3, 4]. However, only two of them are usually identified in laboratory plasmas. For simplicity, assuming the presence of only bulk ions and electrons, when the collisionality of both species is such that the radial particle flux of the ions needs to be reduced in order to satisfy ambipolarity, the ambipolar electric field typically points radially inward and $E_r < 0$. If, on the contrary, the electron radial particle flux needs to be retarded to fulfill ambipolarity the radial electric field points radially outwards, $E_r > 0$. These two situations are referred to as ion and electron root regimes respectively. In general, standard neoclassical theory predicts ion root conditions for all collisionalities when the ion and electron temperatures are comparable, $T_i \sim T_e$, and fairly large and positive (electron root) E_r values at low collisionality with strongly localized electron heating that leads to $T_e \gg T_i$, see e.g. [5, 6]. The concern for the intrinsic character of the impurity accumulation in stellarators and ion root conditions has been traditionally tight together, since the inward convection related to E_r can, for sufficiently high Z_a , exceed in most situations the outward counterparts driven by the temperature and density gradients. This has also been observed in numerous stellarator experiments, see e.g. [7] and references therein.

However, this simple explanation concerning impurity accumulation has been broadened in recent years motivated by a few experiments that question it, like the hollow impurity density profiles observed in LHD [8] or the exceptionally low impurity confinement time of the HDH mode in W7-AS plasmas [9]. For decades it has been known that a variation of the electrostatic potential over the flux surface $\Phi_1 = \Phi_1(r, \theta, \phi)$ can be relatively large for low collisionality plasmas in non-omnigeneous stellarators [3, 10, 11]. Here θ and ϕ are some angular poloidal and toroidal coordinates, respectively. This piece of the electrostatic potential is necessary in order to restore quasi-neutrality over the flux surfaces, which the cumulative effect of the non-vanishing bounce-averaged radial displacement of the particle drift orbits violates. Although it can be in most situations negligible for main ion and electron transport, the importance of Φ_1 for impurities resides in the fact that the radial component of the $E \times B$ drift, $\mathbf{v}_{E1} = -\nabla\Phi_1 \times \mathbf{B}/B^2$, can become of the same order as the radial component of the magnetic drift \mathbf{v}_m , basically because the latter scales as Z_a^{-1} while the former does not. Consequently, its role as source of radial transport can become as important as the inhomogeneous confining magnetic field for sufficiently high charge state. Since the first numerical calculations of Φ_1 [12] performed with the code EUTERPE [13, 14] and the experimental measurement in a stellarator [15], other works have followed this line: the estimation of its effect on the radial flux of impurities for some selected ion-root plasmas for different stellarator configurations in ref. [1]; the analytical development of the formalism [16] and the code (KNOSOS) [17] that integrates the drift kinetic equation and transport quantities of interest, including Φ_1 , for optimized stellarators; new LHD impurity plasmas analyzed under the effect of Φ_1 with the SFINCS code [18, 19], including the self-consistent modification of E_r by Φ_1 and including non-trace impurities [20]. Apart from these works, others have looked into the screening of impurities in stellarators, like ref. [21] where high T_i plasmas with negative but small $|E_r|$ are shown to coexist with outward impurity flow. Finally, ref. [22] has analytically addressed the radial particle flux of highly collisional impurities in low collisional bulk plasmas, concluding that in the case without Φ_1 , the radial transport of impurities may only weakly depend on E_r and temperature screening can arise; and ref. [23] where the previous derivation is generalized including Φ_1 , which makes the impurity radial particle flux to depend strongly on E_r .

The conclusions from the works dealing with Φ_1 [1, 17, 20] coincide on their prediction about its magnitude, that reaches for LHD values of up to $e\Delta\Phi_1/T_i \sim 0.1$, with $\Delta\Phi_1 = (\Phi_1^{\max} - \Phi_1^{\min})$ and Φ_1^{\max} and Φ_1^{\min} the maximum and minimum values, respectively, of the potential over a given flux surface. The direction and magnitude of the impact of Φ_1 on the impurity radial transport is not trivial. It depends on the charge state of the impurities, the collisional regime where the impurity is, how its distribution function couples to Φ_1 , etc. However, based on the available numerical simulations it can be stated without too much lack of generality that variations of that magnitude undeniably introduces a strong correction to the standard neoclassical prediction in LHD, even considering low- Z impurities like carbon. For TJ-II similar values of the

normalized potential variation are also predicted [1], despite the higher collisionality of its plasmas. Moreover, the estimations in TJ-II qualitatively agree with the experimental measurements of the plasma floating potential difference at the plasma edge [15]. Regarding W7-X, the variations are typically shown one order of magnitude lower than those for LHD plasmas at comparable collisionality. However, as noted below only few simulations are available, in particular, for the magnetic configurations and plasma parameters from the experimental campaigns.

The present work aims at broadening the scanned parameter space with a comparative view between ion root and electron root conditions in TJ-II and W7-X, with the focus mainly on the second of these regimes. There are several reasons for this: first, all the numerical effort has looked so far into ion root plasmas, with the underlying hope that Φ_1 could, at least, cancel the predicted E_r -driven inward pinch. A similar analysis for electron-root plasmas is missing despite the fact that Φ_1 can indeed be larger than in ion-root for the same absolute value of E_r , as pointed out in [15]; second, although its impact is predicted to be large for impurities, the value of Φ_1 is still small compared to the lower order part of the potential Φ_0 , and its direct detection is instrumentally difficult. In the present work, under the light of recent Doppler reflectometry (DR) measurements of the radial electric field in TJ-II, where strong differences over the same flux surfaces have been found under electron root conditions, we investigate whether the radial dependence of the calculated Φ_1 can explain those differences; and finally, since the configuration and parameter space of W7-X is rather large [24], the results obtained for the few configurations and parameters considered in [1, 20] should not be generalized. In the present work, we have based our calculations in typical parameters of OP1.1 [25] Core-Electron-Root-Confinement (CERC) plasmas considering a configuration with large effective ripple. We show numerically that Φ_1 can then be as large as in the reported LHD cases. This exercise has also been performed considering adiabatic and kinetic electrons, in order to provide explicitly a validity check for the adiabatic electron approximation, that for codes like EUTERPE can result in considerably less computation time.

After this section, a brief overview of the equations and tools employed are described in section 2. The TJ-II results, both numerical and experimental, are presented and discussed in section 3. The numerical analysis for W7-X CERC conditions is shown in section 4. Finally, the conclusions are summarized in section 5.

2. Equations and numerical methods

In this section we give an overview of the numerical method, the relevant equations of the problem and the numerical code used, EUTERPE [13, 14]. The content of this section concerns the neoclassical version of the code. For a more complete description of how the present problem is approached we refer the reader to section 2 of ref. [1].

Other aspects dealing with the neoclassical version can be found in refs. [26, 12, 27], and those closer to the numerical implementation in refs. [28, 29, 30].

EUTERPE is a δf particle-in-cell (PIC) Monte Carlo code. For a given kinetic species, it considers a splitting of the distribution $f = f_0 + f_1$, with f_0 an analytically known expression with the role of a control variate, which does not have to be necessarily linked to any approximation. The code solves for each of the kinetic species of the problem the equation for the f_1 part: $df_1/dt = -df_0/dt + C(f)$, with $C(f)$ a collision operator. The choice of phase space coordinates is the following: in real space, in order to characterize the guiding center position \mathbf{R} of the Monte Carlo markers, the magnetic PEST [31] poloidal and toroidal angles θ and ϕ , and a flux surface label r are employed. In velocity space the parallel component of the velocity v_{\parallel} and normalized magnetic moment $\mu = v_{\perp}^2/2B$ are considered. Here $f_0 = f_M \exp(-Ze\Phi_1/T)$, with $f_M = [n_0/(2\pi)^{3/2}v_{th}^3] \exp[-(v_{\parallel}^2 + v_{\perp}^2)/v_{th}^2]$ the Maxwellian distribution, v_{\perp} the perpendicular component of the velocity, $n_0 = n_0(r)$ the constant part of the density of the flux surface, T the temperature, $v_{th} = \sqrt{2T/m}$ the thermal speed, m the mass and B the magnetic field strength. With these definitions, the kinetic equation takes the form:

$$\frac{\partial f_1}{\partial t} + \dot{\mathbf{R}} \cdot \nabla f_1 + \dot{v}_{\parallel} \frac{\partial f_1}{\partial v_{\parallel}} = -f_M (\mathbf{v}_m + \mathbf{v}_{E1}) \cdot \nabla r \left[\frac{n'}{n} + \frac{Ze}{T} \Phi'_0 + \left(\frac{mv^2}{2T} - \frac{3}{2} + \frac{Ze}{T} \Phi_1 \right) \frac{T'}{T} \right] + C(f). \quad (3)$$

The overdot $\dot{}$ denotes differentiation with respect to time t . Finally, the following equations of motion enter the left-hand-side of eq. (3):

$$\dot{\mathbf{R}} = v_{\parallel} \mathbf{b} + \frac{\mathbf{b} \times \nabla \Phi_0}{B}, \quad (4)$$

$$\dot{v}_{\parallel} = -\frac{\mu}{m} \mathbf{b} \cdot \nabla B - \frac{v_{\parallel}}{B^2} (\mathbf{b} \times \nabla B) \cdot \nabla \Phi_0 - \frac{Ze}{m} \mathbf{b} \cdot \nabla \Phi_1, \quad (5)$$

$$\dot{\mu} = 0, \quad (6)$$

with $\mathbf{b} = \mathbf{B}/B$. In order to obtain Φ_1 , quasi-neutrality among all the species is imposed up to first order: $\sum_a Z_a e n_a = 0$, with $n_a = n_{0a}(r) \exp(-Z_a e \Phi_1/T_a) + n_{1a}$ the density of the different species. Considering singly charged bulk ions (i) and electrons (e) and assuming $e\Phi_1/T \ll 1$, quasi-neutrality yields:

$$\Phi_1 = \frac{T_e}{e} \left(n_{0e} + n_{0i} \frac{T_e}{T_i} \right)^{-1} (n_{1i} - n_{1e}). \quad (7)$$

Note that in ref. [1] the assumption of adiabatic electrons, i.e. $n_e \approx n_{0e}(r) \exp(e\Phi_1/T_e)$, implies that on the right-hand-side of expression (7) only n_{1i} appears. In the present work, in section 4, this approximation is relaxed and the results with adiabatic and kinetic electrons are compared with each other.

Another difference between ref. [1] and the present work is the treatment of the collision operator $C(f)$. While in ref. [1] pitch angle scattering collisions without momentum conservation were applied, in the present work, a momentum-restoring field particle term similar to that implemented in other codes [32, 33] is added to the self-collisions. The detailed description of the conservation scheme implemented in EUTERPE can be found in ref. [34] but we reproduce it here for convenience. The collision operator that describes the self-collision of any species can be expressed as

$$C(f) = C_{\text{tp}}(f) + C_{\text{fp}}(f), \quad (8)$$

where $C_{\text{tp}}(f) = C(f_1, f_M)$ is the usually referred to as test-particle term, that describes the collisions of the perturbed part of the distribution function against the background part, and $C_{\text{fp}}(f) \equiv C(f_M, f_1)$ is the field particle term, which captures the background reaction. In the simulations presented in next sections, both for the bulk ion and electron self-collisions, the test-particle term used has been the pitch angle collision operator:

$$C_{\text{tp}}(f_1) = \frac{\nu}{2} \frac{\partial}{\partial \xi} (1 - \xi^2) \frac{\partial}{\partial \xi} f_1, \quad (9)$$

with $\xi = v_{\parallel}/v$ the pitch-angle variable, v the particle velocity and ν the deflection collision frequency of the colliding species

$$\nu = \nu_0 \frac{\text{erf}(x) - G(x)}{x^3}, \quad (10)$$

and $\nu_0 = ne^4 \ln \Lambda / 4\pi \epsilon_0^2 m^2 v_{th}^3$ for bulk ions with $Z = 1$ and electrons, $x = v/v_{th}$, $\ln \Lambda$ the Coulomb logarithm, erf the error function and G the Chandrasekhar function. On the other hand, the field particle term has the following form in order to fulfill self-adjointness of the collision operator [35],

$$C_{\text{fp}} = [N(\mathbf{v})\mathcal{N} + P(\mathbf{v})\mathcal{P} + E(\mathbf{v})\mathcal{E}] f_M, \quad (11)$$

with

$$N(\mathbf{v}) = \nu - 3\sqrt{\frac{\pi}{8}}\nu_E x^2, \quad (12)$$

$$P(\mathbf{v}) = \nu_s \frac{v_{\parallel}}{v_{th}^2}, \quad (13)$$

$$E(\mathbf{v}) = \nu_E x^2, \quad (14)$$

and $\nu_s = 4\nu_0 G(x)/x$ the slowing down frequency and $\nu_E = [-2\nu + (2 + 1/2x^2)\nu_s]$ the energy-diffusion collision frequency. Evaluating at each spatial bin of the simulation the non-conserved number density ΔN , parallel momentum ΔP and energy ΔE after performing the test-particle collisional step, the coefficients \mathcal{N} , \mathcal{P} and \mathcal{E} are obtained

by imposing conservation of the respective moments of the collision operator (8), which results in

$$-\begin{pmatrix} \Delta N \\ \Delta P \\ \Delta E \end{pmatrix} = \int d^3v f_M \begin{pmatrix} N(\mathbf{v}) & P(\mathbf{v}) & E(\mathbf{v}) \\ v_{\parallel} N(\mathbf{v}) & v_{\parallel} P(\mathbf{v}) & v_{\parallel} E(\mathbf{v}) \\ v^2 N(\mathbf{v}) & v^2 P(\mathbf{v}) & v^2 E(\mathbf{v}) \end{pmatrix} \begin{pmatrix} \mathcal{N} \\ \mathcal{P} \\ \mathcal{E} \end{pmatrix}. \quad (15)$$

Finally, in section 4, where kinetic electrons have also been considered, the collision operator employed for the electrons colliding against the background ions, assumed to be at rest respect to the former, has been

$$C_{ei}(f_{1e}) = \frac{\nu_{ei}}{2} \frac{\partial}{\partial \xi} (1 - \xi^2) \frac{\partial}{\partial \xi} f_{1e}, \quad (16)$$

with $\nu_{ei} = n_i e^4 \ln \Lambda / 4\pi \epsilon_0^2 m_i^2 v_e^3$, n_i the bulk ion density, v_e velocity of the electrons and m_e their mass.

3. Potential variations in TJ-II: comparison between ion- and electron-root plasmas

3.1. TJ-II Doppler reflectometry system

TJ-II is a heliac-type stellarator where, for the standard configuration considered for this work, the average magnetic field is 0.95 T on axis, the rotational transform is $\iota \approx 1.5$ at the center of the plasma and 1.6 approximately at the edge and the effective minor radius and major radius are $a = 0.2$ m and $R_0 = 1.5$ m, respectively. The available heating power consists of two gyrotrons delivering 300 kW each (operated both in X-mode at the second harmonic of the electron cyclotron frequency) and two NBI heating systems, one co- and another counter-injecting each a port-through power of up to 700 kW. For the results presented below, only ECH on-axis was used. With this heating scheme the central electron density typically reaches values of $n_e \approx 0.5 - 1 \times 10^{19} \text{ m}^{-3}$, the electron temperature is $T_e \approx 1 - 2$ keV and the ion temperature $T_i \approx 80 - 100$ eV.

For the experimental results discussed in this section the technique used has been Doppler reflectometry (DR). It allows the measurement of density fluctuations and their perpendicular rotation velocity at different turbulence scales, with good spatial and temporal resolution. From the perpendicular rotation velocity the radial electric field, the central quantity in this section, can be obtained. The DR in operation at TJ-II [36] works in a frequency hopping mode in the Q-band: 33-50 GHz, covering typically the radial region from $r/a = 0.6$ to $r/a = 0.9$. Its front-end consists of a compact corrugated antenna and an ellipsoidal mirror. The mirror can be tilted to probe different perpendicular wave-numbers of the turbulence in the range $k_{\perp} \approx 1 - 14 \text{ cm}^{-1}$, at different plasma regions poloidally separated, as both positive and negative probing beam angles with respect to normal incidence can be selected, see fig. 1. Assuming that the electron density is constant on each flux surface, this characteristics makes possible to access

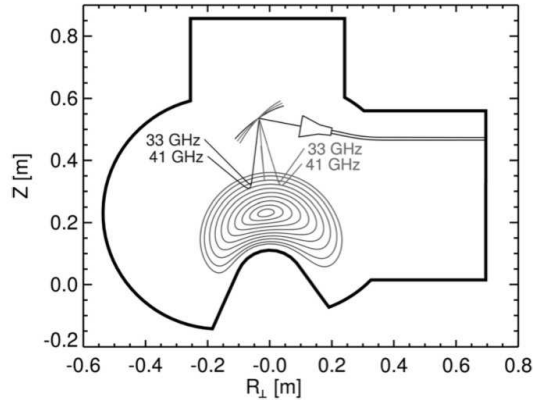


Figure 1. Schematic representation of the TJ-II vacuum vessel with DR antenna-mirror arrangement showing the two plasma regions that can be probed by the system. Here $R_{\perp} = R - R_0$, with R the cylindrical radial coordinate used below and R_0 the major radius of the device.

different points of measurement over the same flux surface. Apart from its interest for studying the spatial localization of instabilities predicted in stellarators by gyro-kinetic simulations [13, 37, 38], for the results presented in this work this feature has been exploited to characterize the radial electric field measured on the left and right regions with respect to the incidence angle where the launched beam is normal to the last closed flux surface. Throughout the present section these regions are referred to as “left” and “right” regions, see fig. 1.

3.2. Experimental and numerical results

Two pairs of TJ-II discharges are considered. The main difference between them is the sign of the radial electric field. The first couple of discharges (#43387 and #43388) are representative for ion root regime while the second couple of discharges (#43391 and #43392) are in electron root. The plasma parameters for each of these pairs are represented in figs. 2 (left) and 2 (right) respectively. The difference in the density profiles determines what regime is accessed. TJ-II plasmas exhibit this ion-to-electron root change when the line-averaged density, obtained with a microwave interferometer [39], is close to the critical value of $\bar{n}_e^{\text{cr}} \sim 0.6 \times 10^{19} \text{ m}^{-3}$ (for the standard magnetic configuration and the used heating power), which standard neoclassical calculations capture without difficulty, see e.g. [40, 41]. The characteristic of the DR analysis that has motivated the numerical simulations is the difference that the radial electric field value for each set of profiles, shows when the measurement is taken on the left probing region and on the right. Or in other words, the different values of the radial electric field measured at different points over the same flux surface.

The radial electric field was obtained for the first discharge of each pair (this is for the shots #43387 and #43391) on the left side of the DR measurement plane. For the

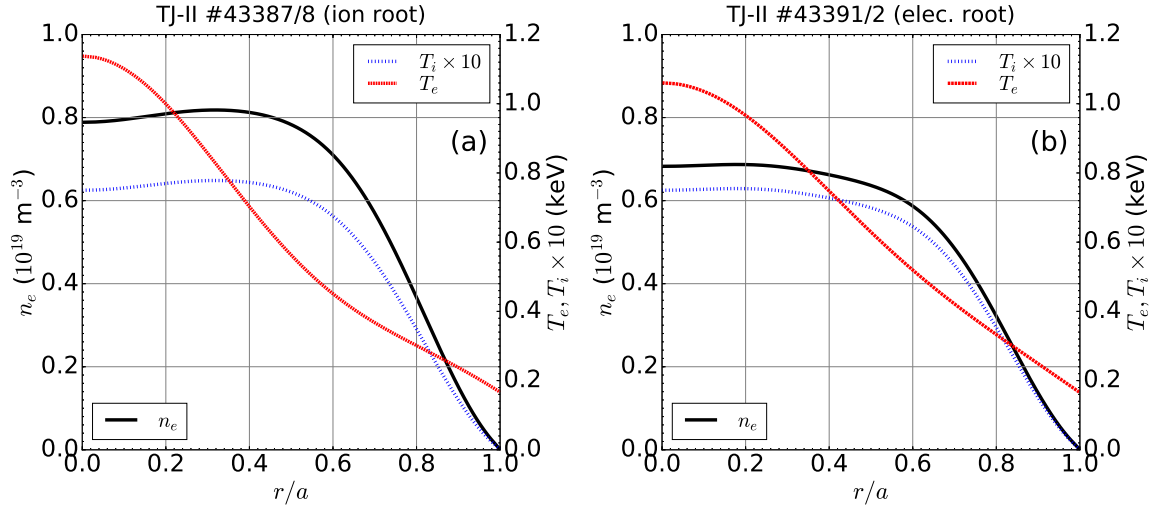


Figure 2. Left: radial profiles of electron density (n_e , solid black line), electron temperature (T_e , dashed red line) and ion temperature multiplied by 10 (T_i , dotted blue line) considered for the EUTERPE simulations based on the TJ-II discharges #43387 and #43388 and the data from the Thomson Scattering diagnostic (n_e and T_e) and the NPA system (T_i) systems. Right: same quantities as on the left but considering the TJ-II discharges #43391 and #43392.

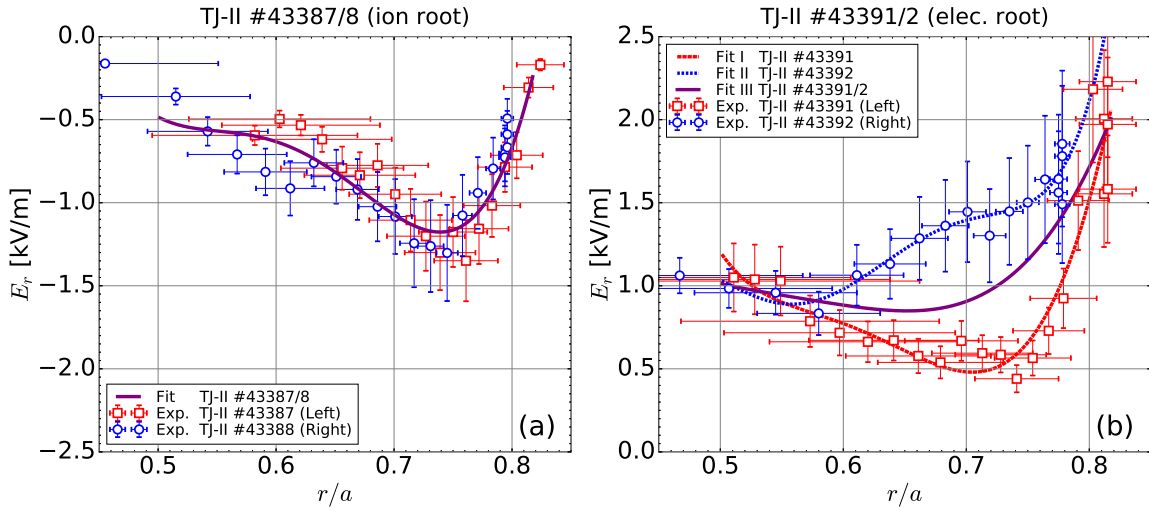


Figure 3. Left: radial electric field E_r as a function of the normalized effective radius for the TJ-II ion root plasmas, discharges #43387 and #43388. Right: the same but for the electron root plasmas from discharges #43391 and #43392. In both cases the measurements performed on the left and right sides of the DR measurement plane are represented with red squares and blue circles, respectively. The solid lines correspond to the input radial electric field profiles used for the Φ_1 EUTERPE simulations.

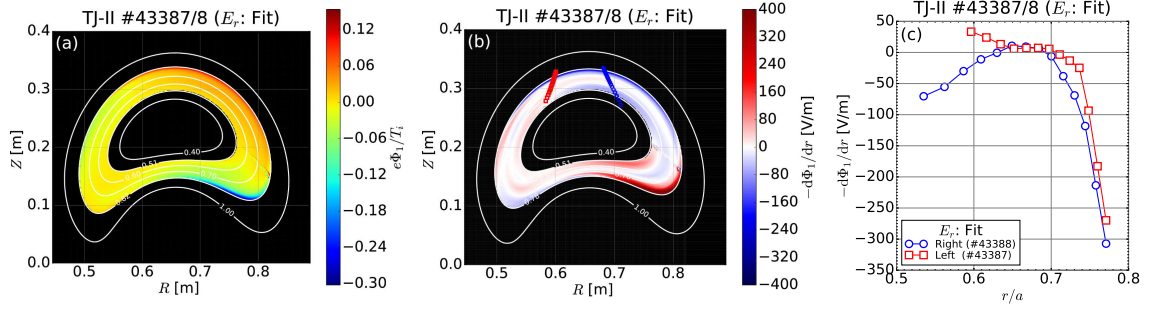


Figure 4. For the ion root conditions TJ-II plasmas: (a) potential variation normalized to the ion temperature $e\Phi_1/T_i$ at the Doppler reflectometry probing plane in the range of simulated radii; (b) Over the same plane, radial electric field component $-d\Phi_1/dr$, together with the specific positions of measurement on the left and right DR probing regions, estimated with ray tracing; (c) Value of $-d\Phi_1/dr$ at those positions where, as before, red squares and right blue circles correspond to the estimations along the left and right measurement positions respectively.

second of the discharges of each pair (this is for shots #43388 and #43392) the DR beam was launched to measure the radial electric field on the right side. It is worth recalling that the radial electric field provided by the Doppler reflectometer, E_r^{DR} , is obtained from the measured plasma background perpendicular flow u_\perp and relates to it as $E_r^{\text{DR}} = u_\perp B$ (B the modulus of the local magnetic field at the point where the beam is reflected). Assuming the phase velocity of density fluctuations much smaller than the $E \times B$ flow velocity, $\mathbf{v}_{E0} = E_r \nabla r \times \mathbf{B}/B^2$, u_\perp is assumed to be equal to the latter. Typically the value provided E_r^{DR} , is that of the local radial electric field, which carries with the local dependence of the flux expansion term ∇r . This term is comparable in the two plasma regions the system can access, and cannot lead to large differences in the local radial electric field. But, since the present work focuses on the different value of the radial electric field at points located over the same flux surface, the modulus of the flux expansion term has been divided out from the experimental E_r^{DR} in order to work with, strictly speaking, the supposedly flux function quantity E_r . This is indeed the quantity neoclassical codes require as input. The radial electric field is represented as a function of the normalized effective radius r/a in fig. 3 (left) for the ion root discharges and 3 (right) for the electron root discharges. The points with errorbars show the experimental data, and the solid lines correspond to different fitted curves used in the EUTERPE simulations presented in next subsection. The values obtained at the left side of the plane of measurement are represented with red open squares while those taken at the right side are represented by blue open circles. Note that the DR system can measure over different flux surfaces by scanning the frequency of the launched microwaves. Due to their X-mode polarization and the dependence of the X-mode cutoff not only on the electron density but also on the magnetic field strength, the accessible radial range when the beam is oriented toward the left and right regions of the plane of measurement is not exactly the same. This fact is reflected in the measurements shown in fig. 3 and when the numerical analysis is addressed considering the estimated mea-

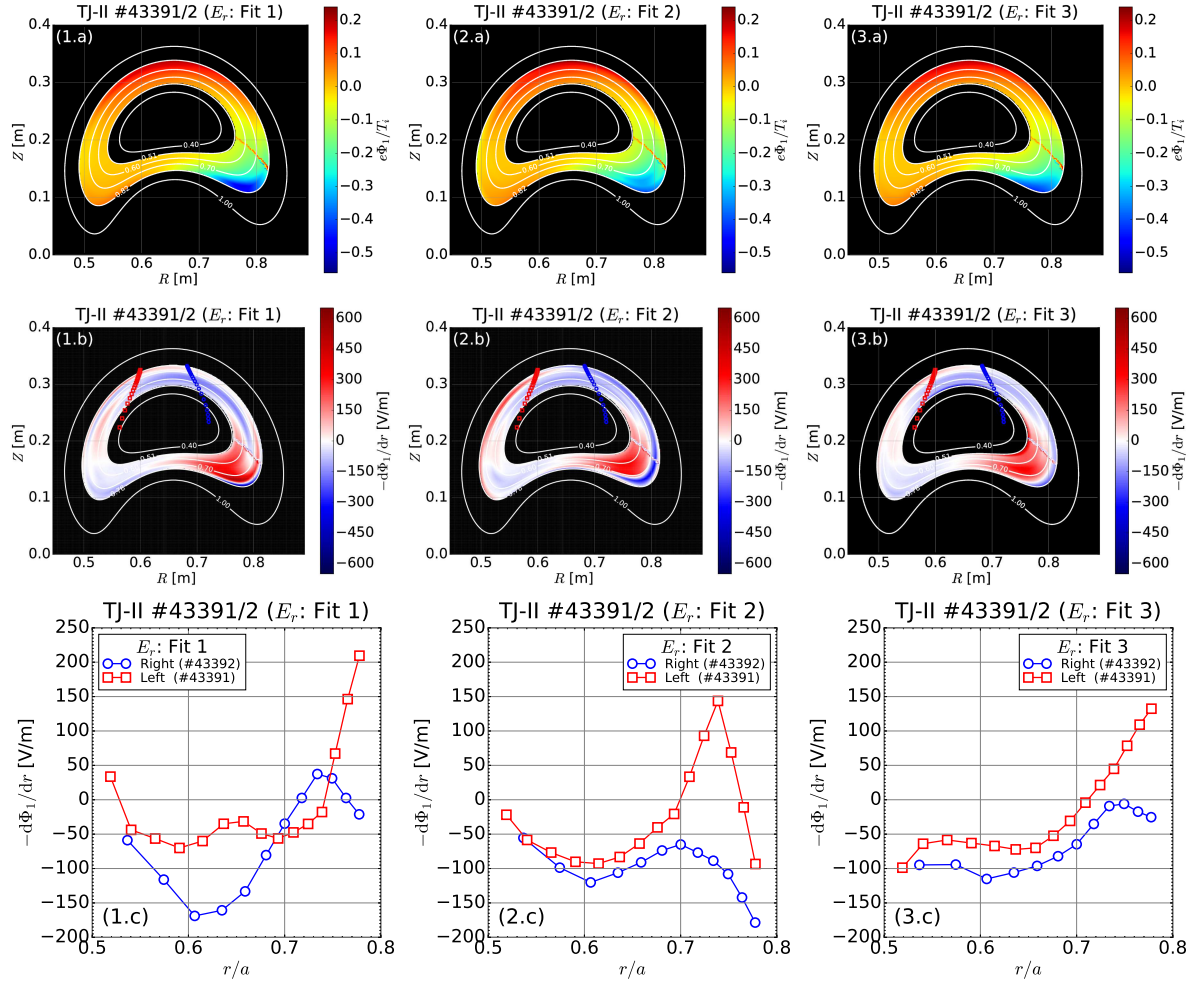


Figure 5. For the electron root conditions TJ-II plasmas: (1-3.a) potential variation normalized to the ion temperature $e\Phi_1/T_i$ at the Doppler reflectometry probing plane in the range of simulated radii, from left to right for the input E_r denoted as fit 1 to 3 in fig. 3(b); (1-3.b) over the same plane, first order radial electric field $-d\Phi_1/dr$, together with the specific positions of measurement on the left and right DR probing regions, estimated with ray tracing for the three E_r fits considered; (1-3.c) value of $-d\Phi_1/dr$ at those positions where, as before, red squares and right blue circles correspond to the estimations along the left and right regions, respectively.

surement positions with ray tracing techniques. As it is observed in fig. 3 (left), for the ion-root plasmas (shots #43387/8) the difference between the radial electric field measured at each side is small, in all the accessible radial domain. Only around $r/a = 0.6$ a slight separation between them can be appreciated. On the contrary, under electron root conditions (shots #43391/2), see fig. 3 (right), the measured radial electric field is appreciably larger on the right side than on the left side on a wide portion of the accessed radial range. In the interval $r/a = 0.6 - 0.8$ discrepancies of up to 1 kV/m can be observed. In the numerical analysis that follows we try to quantify to what extent the radial dependency of the potential Φ_1 can introduce corrections in the total radial electric field through the term $-\Phi'_1 = -d\Phi_1/dr$.

For the numerical simulations different fitting curves for the input ambipolar electric field have been considered. They are depicted with solid lines in fig. 3. For the ion root scenario only one case has been used while for electron root three have been considered, due to the ambiguity in the choice of E_r given the disparate values measured at each measurement region. One of the curves considers the data measured on the left side of the probing plane (“fit 1”), another the data measured on the right side of the plane (“fit 2”) and a third one the mean value of the previous two (“fit 3”).

The numerical results for the ion root case are shown in figs. 4(a) to (c), where the following quantities are represented: (a) the potential variation Φ_1 in a corona of the measurement plane that covers approximately the same radial range as the experimental data; (b) the radial electric field term $-\Phi'_1$ resulting from the potential represented in the previous figure. The Doppler reflectometry measurement positions on the right and left regions are indicated with red and blue points (these positions have been obtained with the ray tracing code TRUBA [42]); (c) $-\Phi'_1$ at the positions indicated in the previous plot. The results estimated on the left regions are indicated in red color, while those concerning the right side are indicated in blue. In fig. 4(a) it is observed that the normalized potential $e\Phi_1/T_i$ takes at different poloidal positions near the outermost radii of the simulated region minimum and maximum values of around -0.3 to 0.15 , respectively. This leads the modulus of Φ'_1 to reach up to 400 V/m approximately, comparable to the input E_r at that position, see fig. 3(a). In such situation, neglecting the radial drift $\mathbf{b} \times \nabla\Phi_1/B$ at the time that the tangential drift $\mathbf{b} \times \nabla\Phi_0/B$ is retained in eq. 4 is not justified. Then, apart from the fact that the radial region with $r/a \gtrsim 0.7$ has exceptionally large values of Φ'_1 , further quantitative conclusions can difficultly be drawn from these results. On the other hand at more internal r/a regions, where Φ_1 and Φ'_1 have more moderate values, one can observe in fig. 4 (c) that there is barely no difference between the value of $-\Phi'_1$ on the left measurement positions and those on the and right region. Only at around $r/a = 0.6$ the curves in fig. (c) separate from each other a few tens of V/m – like in the experimental measurements, see fig. 2(a) – which is well below the value of the ambipolar electric field at that position $E_r \approx -600$ V/m. In that sense the numerical results agree relatively well with the experiment.

For the electron-root plasmas the same (a) to (c) plots are represented from top to bottom in the set of figs. 5, for each of the input E_r considered for EUTERPE in a different column. Looking at the figs. (1-3.c), in contrast to the ion-root case, a more appreciable difference than for the ion root plasmas is observed between the results for the left and right regions. In the three cases the correction term $-\Phi'_1$ would make the total radial electric field larger on the left side than on the right side, as the curve of Φ'_1 indicating the left side values is situated almost at all radii above the curve indicating the values on the right region. The difference between the results with different input E_r are given only on the location where the maximum differences on $-\Phi'_1$

are found. Considering the fit 1, the difference reaches up to values of around 200 V/m, and these take place in the interval $r/a = 0.6 - 0.7$ and the outermost radial region. For the fit 2 differences of up to around 250 V/m, larger on the left than on the right side, are observed at around $r/a \sim 0.75$; and finally fit 3 leads to differences that only show up at the outermost represented radii, reaching values of around 200 V/m. The numerical difference for the three cases considered are neither as large as those found in the DR measurements shown in fig. 3 (right) nor the sign coincides numerically and experimentally. In the simulations the radial electric field becomes larger on the left than on the right probing regions, while in the experiments the opposite happens. However, out of the measurement positions, along any flux surface contour over the probing plane much larger values of $-\Phi'_1$ are achieved. See for instance the reddish areas at the bottom right part of the DR section and the top blue areas the contour $r/a = 0.5$ passes through in fig. 5 (1-3.b) plots. As it has been already discussed regarding the outermost flux surfaces of the ion-root case, these large deviations cast strong doubts about the applicability of the trajectories, eq. (4)-(6) assumed in our simulations, since all terms related to Φ'_1 have been neglected. The correction to the total radial electric field arising from $-\Phi'_1$ represents in these electron root TJ-II plasmas a significant fraction compared to the input ambipolar electric field. In contrast to the ion-root case, where this happened near the outermost radial boundary only, in this electron-root example the problem shows up at almost any of the represented flux surfaces regardless of the considered profile of E_r . This limits our conclusion substantially, and reduces it to the statement that in TJ-II electron root plasmas the magnitude of Φ_1 and related contribution to the total radial electric field $-\Phi'_1$ can become locally a non-negligible fraction of Φ_0 and E_r , respectively.

4. Potential variations in W7-X: CERC plasmas and effect of kinetic electrons

Potential variations have so far been estimated small in W7-X plasmas and its impact on impurity transport negligible. However, these conclusions, drawn from the results presented in refs. [1, 20], cover still a very narrow parameter and configuration window of W7-X. In particular all plasmas studied in those references are ion root plasmas foreseen during the future W7-X operation phase OP2. The calculations in ref. [1] were performed for one of the W7-X configurations with lowest neoclassical transport, whose low effective ripple, the target figure of merit for the neoclassical optimization and design of W7-X, is lower than in the configurations for which most of the experiments have been performed so far. The case studied in this work widens the parameter window considering CERC plasma parameters from the operation phase OP1.1 [43], in particular the physics programme 20160309.010 at the time $t = 0.320$. The radial profiles based on that programme and instant, used for the simulations discussed below are represented in fig. 6 (left). The represented profiles are fitted to the Thomson Scattering system [44] data for the electron density n_e and temperature T_e , while the bulk ion density T_i

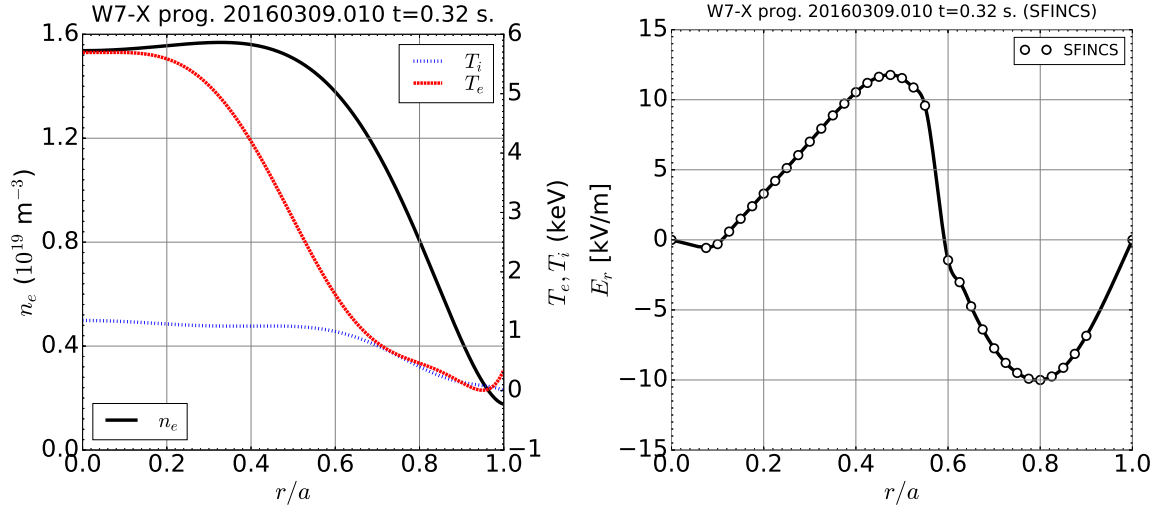


Figure 6. (a) Electron density (n_e , solid black line), electron temperature (T_e , dashed red line) and ion temperature (T_i , dotted blue line) considered for the EUTERPE simulations based on those of W7-X programme 20160309.010 at $t = 0.32$ ms measured with the Thomson Scattering (n_e and T_e) and the XICS (T_i) systems. (b) ambipolar radial electric field obtained with the SFINCS code (dots) considering the profiles on the left, and the curve used as input for EUTERPE.

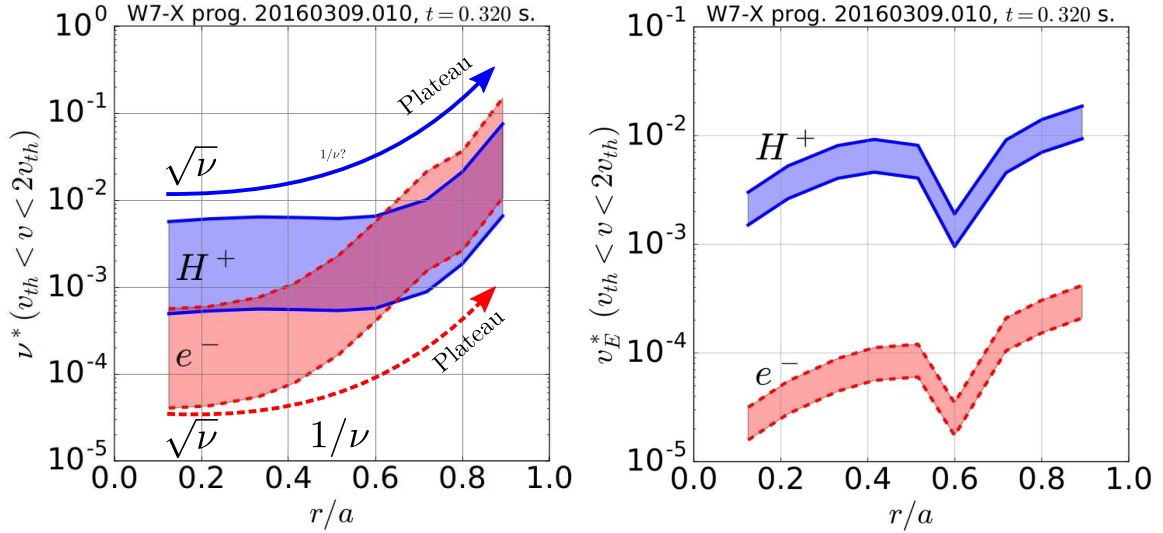


Figure 7. Left: normalized collision frequency as a function of the normalized effective radius for the electrons (red shadowed area) and main ions (blue shadowed area) with velocities in the range of one and two thermal velocities considering the profiles of fig. 6(a). Right: normalized $E_r \times B$ velocity for electrons (red shadowed area) and main ions (blue shadowed area) with velocities in the range of one and two thermal velocities considering the profiles of fig. 6(a) and (b).

considers the XICS [45] experimental data. The radial profile of E_r used as EUTERPE input has been provided by the SFINCS code and is represented in fig. 6 (right).

The reasons for choosing this plasma are the following. On the one hand, it is an example of CERC plasma [46] where a root transition takes place. E_r is positive (electron root) at the inner core and negative (ion root) at the outer part of the core and edge. This feature is interesting since, as pointed out in [15], under ion root conditions the thermodynamic force related to the ambipolar radial electric field opposes to the density and temperature gradients, while in electron root all thermodynamic forces have in general for the ions (except deeply hollow profiles, which is not the case here) the same sign. This leads to a larger source term in the drift kinetic equation that forces the perturbed part of the distribution function f_{1i} to be larger. Since the lack of quasi-neutrality among the charge density related to this piece of the distribution function is what gives rise to the potential Φ_1 , this reasoning should lead to expect larger Φ_1 too. In addition, the change in the direction of the $E \times B$ precession from electron to ion root should introduce appreciable changes on the phase of the potential. These two statements can be checked by comparing how Φ_1 looks on each side of the radial electric field root transition.

Furthermore the fact that the temperature of the electrons is significantly higher than that of the ions leads to a situation where the electron contribution ECH to Φ_1 eventually may become important. Note that in ref. [1] the electrons are considered adiabatic, based on the condition $T_i \sim T_e$ and the higher density of the plasmas there, and thus the electron contribution to Φ_1 is neglected. In order to know whether the electrons may contribute to Φ_1 , let us recall first that for a given magnetic configuration and for one single kinetic energy or velocity v , the parameters to find in which collisional regime each species is, are the normalized $E_r \times B$ drift velocity $v_E^* = E_r/vB_0$ and the normalized collision frequency $\nu^* = R_0\nu/(\nu v)$. See for instance ref. [47], where several configurations are considered and the main thermal transport matrix coefficients are represented as a function of ν^* for different values of v_E^* . In particular, in the scalings depicted for the normalized transport matrix coefficient D_{11}^* , helpful visual references of the collisionality interval at which the $1/\nu$ scaling begins and when transits to the $\sqrt{\nu}$ regime are found. This so-called mono-energetic view is somewhat limited since the Maxwellian velocity distribution function covers a range of velocities and not just one. In fig. 7 the range of ν^* and v_E^* values as a function of r/a are represented for electrons and ions (H^+) with velocity between $v = v_{th}$ and $v = 2v_{th}$, considering the plasma parameters of fig. 6. Looking at the values of ν^* and v_E^* for the ion parameters and comparing with the scanned ranges in ref. [47] for W7-X, one can conclude that the ions should mostly be in the $\sqrt{\nu}$ regime at the innermost radial positions and in the plateau regime at the edge, passing through a practically inexistent $1/\nu$ regime. Regarding the electrons, their much lower normalized collisionality compared to that of the ions at the core make them mainly reside in the $\sqrt{\nu}$ regime in that region as well. They also exhibit ν^* values at the edge characteristic of the plateau regime but, contrarily to the ions,

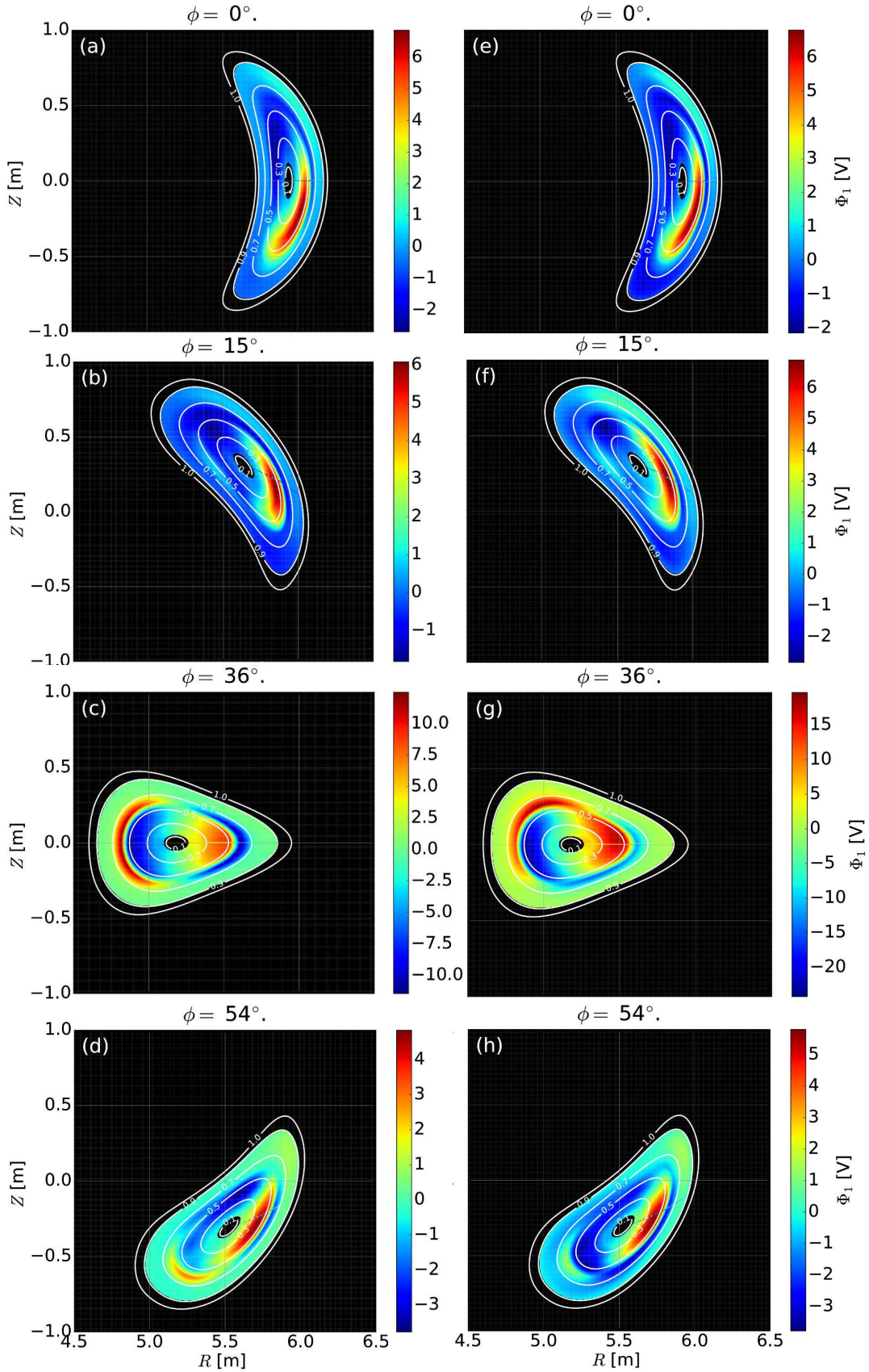


Figure 8. For the simulations with adiabatic electrons (left column) and kinetic electrons (right column), from top to bottom: calculated potential for the W7-X (KJM configuration) at the toroidal planes $\zeta = 0, 15, 36$ and 54° . Note the different color scales on the left and right plots, employed to appreciate the changes in the shape of Φ_1 when considering adiabatic instead of kinetic electrons.

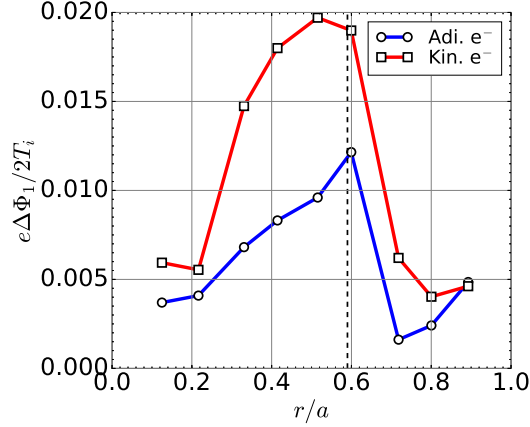


Figure 9. Maximum difference of the potential $\Delta\Phi_1 = \Phi_1^{\max} - \Phi_1^{\min}$ on each of the simulated flux surfaces normalized to the ion temperature T_i as a function of the normalized effective radius r/a for the calculations with adiabatic electrons (circles connected with blue segments) and kinetic electrons (squares connected with red segments). The dashed vertical line indicates the radial position where $E_r = 0$. On the left and right of this line the input radial electric field is positive and negative, respectively.

the much lower v_E^* places them a more robust and wider (in collisionality) $1/\nu$ regime in between. This consequently should make the electrons to necessarily be in a deep $1/\nu$ regime on a radially wide region of the core. Finally, since the perturbed part of the distribution function (and consequently the perturbed part of the density entering in the equation for the potential variation) scales in the $1/\nu$ regime with ρ^*/ν^* while in the $\sqrt{\nu}$ regime is independent of ρ^* and ν^* (with ρ^* the normalized Larmor radius to the stellarator size) [16, 48], the core of these plasmas are particularly favorable to show differences between considering kinetic or adiabatic electrons in the calculations of Φ_1 . This is the numerical comparison presented and discussed in the following paragraph.

The calculations of Φ_1 have been performed for nine radial positions, approximately separated between each other $\Delta r/a = 0.1$. These radii are $r/a = \{0.12, 0.22, 0.33, 0.41, 0.51, 0.60, 0.72, 0.80, 0.90\}$. As in section 3.2, the simulations are local and each considers a different value of the ambipolar radial electric field. In particular the following values are given for each of the flux surfaces just mentioned: $E_r = \{0.59, 3.89, 8.16, 10.95, 11.14, 9.98, -1.38, -8.52, -10.0\}$ kV/m. As it is well known any local code that keeps the tangential $E_r \times B$ drift but neglects the tangential component of magnetic drift, as it is our case, has problems when approaching the value of $E_r = 0$, where an unphysically large magnitude of f_1 is experienced [16, 17]. For this reason we have avoided the exact root transition flux surface where $E_r = 0$. However, the figures of the potential on the toroidal planes have been obtained by interpolation using the value over the simulated flux surfaces, which passes through the entire transi-

tion region. For this reason the results represented in the vicinity of that radius must be taken indicatively. In fig. 8 the potential variation is represented, from top to bottom, for the toroidal planes $\phi = 0^\circ, 15^\circ, 36^\circ$ and 54° . The first of these toroidal planes has the practical interest that a Doppler and a correlation reflectometer probe that plane in order to characterize the experimental radial electric field. At $\phi = 15^\circ$ a second Doppler reflectometer is also installed. The other two planes have been considered since the distance between them in ϕ is one fourth of a the machine period. The first of them corresponds to the frequently represented triangular plane where other essential diagnostics for impurity transport are installed, like the soft-X rays Multi-Camera Tomography System (XMCTS) [49] or the bolometry cameras [50]. The difference between the figures on the left, with labels (a)-(d), and on the right, with labels (e)-(h), is that while the former show the results assuming adiabatic electrons, the latter do it for the cases considering kinetic electrons. First of all, note that the range in the color scale changes from plot to plot, in order to make appreciable the changes in the shape of the potential, that keeping the same scale for all cross sections would not allow to appreciate. Looking at those color scales and their ranges, it can be seen that the largest Φ_1 values are very localized on the triangular plane, where they become much larger than on the other planes. Second, the size of the potential for the case with kinetic electrons is roughly up to twice as large as the results with adiabatic electrons. This is evident on the triangular plane while on the other the difference is not remarkable. Looking at the potential at the triangular plane, it is also observed that the shape experiences appreciable changes when the electrons are considered as a kinetic species compared to the case with adiabatic electrons. In particular, the negative values of Φ_1 , that in the case with adiabatic electrons 8(c) are located on the low field side (LFS) and below the equatorial plane, are displaced towards the high field side (HFS) when electrons are kinetic 8(g). This is also compatible with what is known about the symmetry properties of Φ_1 [51]. When only the contribution from the ions is considered, since they must be mostly in the $\sqrt{\nu}$ regime, Φ_1 must necessarily have cosine components dominating its spectrum, leading to the clear in-out asymmetry that fig. 8(c) illustrates. When kinetic electrons are considered, since they must, as we have hypothesized, add their contribution from the $1/\nu$ regime, the consequent introduction of sine component leads that in-out asymmetry to blur as 8(g) shows. Other changes in the shape are observed in other planes, although not as clear as on the triangular plane.

Other features can more clearly be observed in fig. 9, where the maximum normalized potential difference ($\Delta\Phi_1 = (\Phi_1^{\max} - \Phi_1^{\min})/2T_i$) is represented. The results are shown for both calculations, with adiabatic electrons and with kinetic electrons. Roughly speaking the potential variation size is shown to be considerably larger in the portion of the plasma in electron root than in that under ion root. In addition, a much larger contribution of the kinetic electron response is observed in the first of these regions than in the second. However, the point located in ion root immediately after the root transition at $r/a = 0.6$ exhibits a large value as well. A vertical line represents

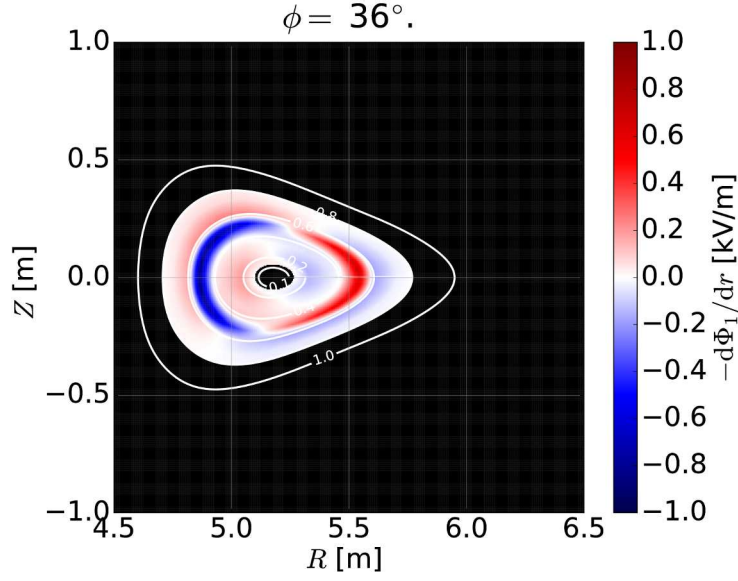


Figure 10. Radial electric field term $\Phi'_1 = -d\Phi_1/dr$ obtained at the toroidal plane $\phi = 36^\circ$, considering the corresponding potential Φ_1 for the case with kinetic electrons represented in fig. 8(g).

the exact position where the root changes. At that point the ambipolar electric field is rather low $E_r = -1.38$ kV/m, compared to the value at the other positions in ion root where $|E_r| > 7$ kV/m. This low value of E_r can be the cause of adding a large contribution to Φ_1 from ions in the $1/\nu$ regime. Another interesting feature results from the large variations at each side of the root transition together with the abrupt change of its phase. To appreciate this one can look at the triangular plane represented in fig. 8(g) for the calculation including kinetic electrons. This change is present at almost any poloidal position in the vicinity of that radius and is given in a relatively narrow region (the two radii simulated immediately before and after the root change are separated by $\Delta r/a = 0.09$). It is then natural to ask whether this can introduce some important contribution to the radial electric field. This correction, $-\Phi'_1$, is represented at the triangular plane, considering kinetic electrons, in fig. 10. Moderate values of a few hundreds of V/m are present on that cross section but near to the root change the value is considerably larger, reaching around 1 kV/m, both positive and negative. In our characteristic trajectories, see eqs. (4)-(6), the $E \times B$ drift related to this component of the radial electric field is not kept to lowest order. This is applicable since, as it happens at almost all positions, E_r is substantially larger than the represented $-\Phi'_1$. However, it becomes of the same order at the innermost simulated radius under ion root conditions (where as above-mentioned E_r was -1.38 kV/m). Then, to this respect the calculations on that specific position should be taken, as well as the conclusions drawn from it, cautiously.

5. Conclusions

The present work has addressed the calculation of the neoclassical potential variation, with the emphasis on electron-root plasmas. The standard configuration for TJ-II and a high mirror configuration of W7-X have been used, considering plasma parameters of discharges from their recent experimental campaigns.

In TJ-II, the Doppler Reflectometry radial electric field measurements and, in particular, the strong difference of its value at different points over the same flux surface, has motivated looking into the radial dependence of Φ_1 and investigating to what extent the term $-\Phi'_1$ can contribute to the total radial electric field. What has been found by numerical simulations agrees qualitatively with the experimental results. The difference in the total electric field that the potential variations can make is large in the electron root cases, although still a non-negligible factor smaller than the experimental one. On the other hand this correction is practically not present in the ion root plasmas, both numerically and experimentally. These conclusions are drawn from the comparison made at the specific measurement positions of the Doppler reflectometry system over the same flux surface. Out of these locations $-\Phi'_1$ is found large both under ion and electron root conditions. This fact questions the applicability of the characteristic trajectories of the simulated particles, since terms containing $-\Phi'_1$ are neglected based on its size compared to $-\Phi'_0$, although *a posteriori* the former is not found that small compared to the latter. This and the possibility that the kinetic electrons could introduce a non-negligible contribution to the potential, as proven in the section by the numerical simulations results for W7-X, are possible reasons than may have frustrated a better agreement.

Regarding W7-X we have considered a configuration with significantly larger effective ripple than the standard configuration analyzed in past works [1]. The plasma parameters correspond to a standard CERC plasma from OP1.1. The analysis has demonstrated that W7-X can access regimes with potential variations significantly larger than what has already been reported. In this occasion the simulations have been performed with adiabatic and kinetic electrons. The comparison between them have shown that the contribution from the kinetic electron response, when the parameters are such that they are likely to be deeply in the $1/\nu$ regime, can be significant in the size and shape of the potential. This occurred mostly in a broad portion of the plasma in electron root, where in addition, the resulting size of Φ_1 was considerably larger than in ion root. Other features have been found, like the localization of these large variations on the triangular plane of W7-X, and the smaller values near the boundaries of the machine period. Interestingly, on that triangular plane, at each side of the root transition and at the closest radii the potential reaches its maximum values. This, together with the fact that the phase is the opposite on one side and the other of the root change, gives rise to a large radial electric field term $-\Phi'_1$.

Acknowledgements

This work has been carried out within the framework of the EUROfusion Consortium and has received funding from the Euratom research and training programme 2014-2018 under grant agreement No 633053. The views and opinions expressed herein do not necessarily reflect those of the European Commission.

This research was supported in part by grants ENE2015-70142-P and FIS2017-88892-P, Ministerio de Economía y Competitividad, Spain.

References

- [1] J. M. García-Regaña, C. D. Beidler, R. Kleiber, P. Helander, A. Mollén, J. A. Alonso, M. Landreman, H. Maaßberg, H. M. Smith, Y. Turkin, and J. L. Velasco. Electrostatic potential variation on the flux surface and its impact on impurity transport. *Nuclear Fusion*, 57(5):056004, 2017.
- [2] I Calvo, F I Parra, J L Velasco, and J A Alonso. Stellarators close to quasisymmetry. *Plasma Phys. and Control. Fusion*, 55:125014, 2013.
- [3] H.E. Mynick and W.N.G. Hitchon. Effect of the ambipolar potential on stellarator confinement. *Nuclear Fusion*, 23(8):1053, 1983.
- [4] D.E. Hastings, W.A. Houlberg, and K.C. Shaing. The ambipolar electric field in stellarators. *Nuclear Fusion*, 25(4):445, 1985.
- [5] H. Maaßberg, R. Burhenn, U. Gasparino adn G. Kühner, and H. Ringler. Experimental and neoclassical electron heat transport in the lmfp regime for the stellarators W7-A, L-2, and W7-AS. *Physics of Plasmas*, 5:3627, 1993.
- [6] H Maaßberg, C D Beidler, and E E Simmet. Density control problems in large stellarators with neoclassical transport. *Plasma Physics and Controlled Fusion*, 41(9):1135, 1999.
- [7] R. Burhenn, Y. Feng, K. Ida, H. Maaßberg, K.J. McCarthy, D. Kalinina, M. Kobayashi, S. Morita, Y. Nakamura, H. Nozato, S. Okamura, S. Sudo, C. Suzuki, N. Tamura, A. Weller, M. Yoshinuma, and B. Zurro. On impurity handling in high performance stellarator/heliotron plasmas. *Nuclear Fusion*, 49(6):065005, 2009.
- [8] K Ida, M Yoshinuma, M Osakabe, K Nagaoka, M Yokoyama, H Funaba, C Suzuki, T Ido, A Shimizu, I Murakami, N Tamura, H Kasahara, Y Takeiri, K Ikeda, K Tsumori, O Kaneko, S Morita, M Goto, K Tanaka, K Narihara, T Minami, I Yamada, and LHD Experimental Group. Observation of an impurity hole in a plasma with an ion internal transport barrier in the Large Helical Device. *Physics of Plasmas*, 16:056111, 2009.
- [9] K. McCormick, P. Grigull, R. Burhenn, R. Brakel, H. Ehmeler, Y. Feng, F. Gadelmeier, L. Giannone, D. Hildebrandt, M. Hirsch, R. Jaenicke, J. Kisslinger, T. Klinger, S. Klose, J. P. Knauer, R. König, G. Kühner, H. P. Laqua, D. Naujoks, H. Niedermeyer, E. Pasch, N. Ramasubramanian, N. Rust, F. Sardei, F. Wagner, A. Weller, U. Wenzel, and A. Werner. New advanced operational regime on the W7-AS stellarator. *Phys. Rev. Lett.*, 89:015001, Jun 2002.
- [10] D. D.-M Ho and R. M. Kulsrud. Neoclassical transport in stellarators. *Physics of Fluids*, 30(2):442–461, 1987.
- [11] C D Beidler and H Maaßberg. Implications of the quasi-neutrality condition for neoclassical transport in stellarators. In *15th International Stellarator Workshop, Madrid*, 2005.
- [12] J. M. García-Regaña, R. Kleiber, C. D. Beidler, Y. Turkin, H. Maaßberg, and P. Helander. On neoclassical impurity transport in stellarator geometry. *Plasma Phys. and Control. Fusion*, 55:074008, 2013.
- [13] V Kornilov, R Kleiber, R Hatzky, L Villard, and G Jost. Gyrokinetic global three-dimensional

- simulations of linear ion-temperature-gradient modes in Wendelstein 7–X. *Physics of Plasmas*, 11:3196, 2004.
- [14] V Kornilov, R Kleiber, and R Hatzky. Gyrokinetic global electrostatic ion-temperature-gradient modes in finite β equilibria of Wendelstein 7–X. *Nuclear Fusion*, 45 (4):238, 2005.
 - [15] M. A. Pedrosa, J. A. Alonso, J. M. García-Regaña, C. Hidalgo, J. L. Velasco, I. Calvo, C. Silva, P. Helander, and R. Kleiber. Electrostatic potential variations along flux surfaces in stellarators. *Nuclear Fusion*, 55:052001, 2015.
 - [16] I. Calvo, F. I. Parra, J. L. Velasco, and J. A. Alonso. The effect of tangential drifts on neoclassical transport in stellarators close to omnigeneity. *Plasma Physics and Controlled Fusion*, 59(5):055014, 2017.
 - [17] J. L. Velasco, I. Calvo, J. M. García-Regaña, F. I. Parra, S. Satake, J. A. Alonso, and the LHD team. Large tangential electric fields in plasmas close to temperature screening. *Plasma Phys. and Control. Fusion (accepted)*, 60(07400), 2018. <https://arxiv.org/pdf/1712.03872.pdf>.
 - [18] M Landreman, H M Smith, A Mollén, and P Helander. Comparison of particle trajectories and collision operators for collisional transport in nonaxisymmetric plasmas. *Physics of Plasmas*, 21:042503, 2014.
 - [19] <https://github.com/landreman/sfincs>.
 - [20] A. Mollén, M. Landreman, H. M. Smith, J. M. García-Regaña, and M. Nunami. Flux-surface variations of the electrostatic potential in stellarators: Impact on the radial electric field and neoclassical impurity transport. *Plasma Phys. Control. Fusion*, 60:084001, 2018.
 - [21] J.L. Velasco, I. Calvo, S. Satake, A. Alonso, M. Nunami, M. Yokoyama, M. Sato, T. Estrada, J.M. Fontdecaba, M. Liniers, K.J. McCarthy, F. Medina, B. Ph Van Milligen, M. Ochando, F. Parra, H. Sugama, A. Zhezhera, The LHD Experimental Team, and The TJ-II Team. Moderation of neoclassical impurity accumulation in high temperature plasmas of helical devices. *Nuclear Fusion*, 57(1):016016, 2017.
 - [22] P. Helander, S. L. Newton, A. Mollén, and H. M. Smith. Impurity transport in a mixed-collisionality stellarator plasma. *Phys. Rev. Lett.*, 118:155002, Apr 2017.
 - [23] I. Calvo, F. I. Parra, J. L. Velasco, J. A. Alonso, and J. M. García-Regaña. Stellarator impurity flux driven by electric fields tangent to magnetic surfaces. 2018. <https://arxiv.org/pdf/1803.05691.pdf>.
 - [24] J Geiger, C D Beidler, Y Feng, H Maaberg, N B Marushchenko, and Y Turkin. Physics in the magnetic configuration space of W7–X. *Plasma Physics and Controlled Fusion*, 57(1):014004, 2015.
 - [25] T Klinger, A Alonso, S Bozhenkov, R Burhenn, A Dinklage, G Fuchert, J Geiger, O Grulke, A Langenberg, M Hirsch, G Kocsis, J Knauer, A Krmer-Flecken, H Laqua, S Lazerson, M Landreman, H Maaberg, S Marsen, M Otte, N Pablant, E Pasch, K Rahbarnia, T Stange, T Szepesi, H Thomsen, P Traverso, J L Velasco, T Wauters, G Weir, T Windisch, and The Wendelstein 7-X Team. Performance and properties of the first plasmas of Wendelstein 7–X. *Plasma Physics and Controlled Fusion*, 59(1):014018, 2017.
 - [26] K Kauffmann, R Kleiber, R Hatzky, and M Borchardt. Global linear gyrokinetic simulations for lhd including collisions. *J. Phys.: Conf. Ser.*, 260 (1):012014, 2010.
 - [27] K Kauffmann. *Including collisions in gyrokinetic tokamak and stellarator simulations*. PhD thesis, Ernst-Moritz-Arndt-Universitaet Greifswald, 2012.
 - [28] M Borchardt, R Kleiber, and W. Hackbusch. A fast solver for the gyrokinetic field equation with adiabatic electrons. *Journal of Computational Physics*, 231(18):6207–6212, jul 2012.
 - [29] R Kleiber and R Hatzky. A partly matrix-free solver for the gyrokinetic field equation in three-dimensional geometry. *Comput. Phys. Commun.*, 183(2):305–308, 2012.
 - [30] R Kleiber, R Hatzky, A Könies, K Kauffmann, and P Helander. An improved control-variate scheme for particle-in-cell simulations with collisions. *Journal of Computational Physics*, 182:1005–1012, 2011.

- [31] R C Grimm, R L Dewar, and J Manickam. Ideal MHD stability calculations in axisymmetric toroidal coordinate systems. *Journal of Computational Physics*, 49:94, 1983.
- [32] S Satake, R Kanno, and H Sugama. Development of non-local neoclassical transport code for helical configurations. *Plasma and Fusion Research*, 3:S1062, 2008.
- [33] T Vernay, S Brunner, L Villard, B F McMillan, S Joliet, T M Tran, A Bottino, and J P Graves. Neoclassical equilibria as starting point for global gyrokinetic simulations. *Physics of Plasmas*, 17:122301, 2010.
- [34] C. Slaby, A. Könies, R. Kleiber, and J. M. García-Regaña. Effects of collisions on the saturation dynamics of taes in tokamaks and stellarators. *Nuclear Fusion*, 58:082018, 2018.
- [35] I G Abel, M Barnes, S C Cowley, W Dorland, and A A Schekochihin. Linearized model fokker-planck collision operators for gyrokinetic simulations. i. theory. *Physics of Plasmas*, 15:122509, 2008.
- [36] T. Happel, T. Estrada, E. Blanco, V. Tribaldos, A. Cappa, and A. Bustos. Doppler reflectometer system in the stellarator TJ-II. *Review of Scientific Instruments*, 80:073502, 2009.
- [37] P. Xanthopoulos, G. G. Plunk, A. Zocco, and P. Helander. Intrinsic turbulence stabilization in a stellarator. *Phys. Rev. X*, 6:021033, Jun 2016.
- [38] J Riemann, R Kleiber, and M Borchardt. Effects of radial electric fields on linear ITG instabilities in W7-X and LHD. *Plasma Physics and Controlled Fusion*, 58(7):074001, 2016.
- [39] M. Sánchez, J. Sánchez, T. Estrada, E. Sánchez, P. Acedo, and H. Lamela. High resolution CO2 interferometry on the TJ-II stellarator by using an ADC-based phase meter. *Review of Scientific Instruments*, 75(10):3414–3416, 2004.
- [40] J. L. Velasco, J. A. Alonso, I. Calvo, and J. Arévalo. Vanishing neoclassical viscosity and physics of the shear layer in stellarators. *Phys. Rev. Lett.*, 109:135003, Sep 2012.
- [41] J L Velasco, J A Alonso, I Calvo, J Arvalo, E Snchez, L Eliseev, S Perfilov, T Estrada, A Lpez-Fraguas, C Hidalgo, and the TJ-II Team. Damping of radial electric field fluctuations in the TJ-II stellarator. *Plasma Physics and Controlled Fusion*, 55(12):124044, 2013.
- [42] M. A. Tereshchenko, F. Castejon, and Á. Cappa. Truba user manual,. *CIEMAT Report*, (1134), 2008.
- [43] R.C. Wolf, A. Ali, A. Alonso, J. Baldzuhn, C. Beidler, M. Beurskens, C. Biedermann, H.-S. Bosch, S. Bozhnikov, R. Brakel, A. Dinklage, Y. Feng, G. Fuchert, J. Geiger, O. Grulke, P. Helander, M. Hirsch, U. Hfel, M. Jakubowski, J. Knauer, G. Kocsis, R. Knig, P. Kornejew, A. Krmer-Flecken, M. Krychowiak, M. Landreman, A. Langenberg, H.P. Laqua, S. Lazerson, H. Maaberg, S. Marsen, M. Marushchenko, D. Moseev, H. Niemann, N. Pablant, E. Pasch, K. Rahbarnia, G. Schlisio, T. Stange, T. Sunn Pedersen, J. Svensson, T. Szepesi, H. Trimino Mora, Y. Turkin, T. Wauters, G. Weir, U. Wenzel, T. Windisch, G. Wurden, D. Zhang, I. Abramovic, S. kslompolo, P. Aleynikov, K. Aleynikova, R. Alzbutas, G. Anda, T. Andreeva, E. Ascasibar, J. Assmann, S.-G. Baek, M. Banduch, T. Barbui, M. Barlak, K. Baumann, W. Behr, A. Benndorf, O. Bertuch, W. Biel, D. Birus, B. Blackwell, E. Blanco, M. Blatzheim, T. Bluhm, D. Bkenhoff, P. Bolgert, M. Borchardt, V. Borsuk, J. Boscary, L.-G. Bttger, H. Brand, Ch. Brandt, T. Bruer, H. Braune, S. Brezinsek, K.-J. Brunner, B. Brnner, R. Burhenn, B. Buttenschn, V. Bykov, I. Calvo, B. Cannas, A. Cappa, A. Carls, L. Carraro, B. Carvalho, F. Castejon, A. Charl, F. Chernyshev, M. Cianciosa, R. Citarella, . Ciupiski, G. Claps, M. Cole, M.J. Cole, F. Cordella, G. Cseh, A. Czarnecka, A. Czermak, K. Czerski, M. Czerwinski, G. Czymek, A. da Molin, A. da Silva, G. Dammertz, J. Danielson, A. de la Pena, S. Degenkolbe, P. Denner, D.P. Dhard, M. Dostal, M. Drevlak, P. Drewelow, Ph. Drews, A. Dudek, G. Dundulis, F. Durodie, P. van Eeten, F. Effenberg, G. Ehrke, M. Endler, D. Ennis, E. Erckmann, H. Esteban, T. Estrada, N. Fahrenkamp, J.-H. Feist, J. Fellingner, H. Fernandes, W.H. Fietz, W. Figacz, J. Fontdecaba, O. Ford, T. Fornal, H. Frerichs, A. Freund, M. Fhrer, T. Funaba, A. Galkowski, G. Gantenbein, Y. Gao, J. Garca Regaa, M. Garcia-Munoz, D. Gates, G. Gawlik, B. Geiger, V. Giannella, N. Gierse, A. Gogoleva, B. Goncalves, A. Gorjaev, D. Gradic, M. Grahl, J. Green, A. Grosman, H. Grote, M. Gruca, C. Guerard, L. Haiduk, X. Han, F. Harberts, J.H.

- Harris, H.-J. Hartfu, D. Hartmann, D. Hathiramani, B. Hein, B. Heinemann, P. Heitzenroeder, S. Henneberg, C. Hennig, J. Hernandez Sanchez, C. Hidalgo, H. Hlbe, K.P. Hollfeld, A. Hlting, D. Hschen, M. Houry, J. Howard, X. Huang, M. Huber, V. Huber, H. Hunger, K. Ida, T. Ilkei, S. Illy, B. Israeli, A. Ivanov, S. Jablonski, J. Jagielski, J. Jelonnek, H. Jenzsch, P. Junghans, J. Kacmarczyk, T. Kaliatka, J.-P. Kallmeyer, U. Kamionka, R. Karalevicius, H. Kasahara, W. Kasperek, N. Kenmochi, M. Keunecke, A. Khilchenko, D. Kinna, R. Kleiber, T. Klinger, M. Knaup, Th. Kobarg, F. Kchl, Y. Kolesnichenko, A. Knies, M. Kppen, J. Koshurinov, R. Koslowski, F. Kster, R. Koziol, M. Krmer, R. Krampitz, P. Kraszewsk, N. Krawczyk, T. Kremeyer, Th. Krings, J. Krom, G. Krzesinski, I. Ksiazek, M. Kubkowska, G. Khner, T. Kurki-Suonio, S. Kwak, R. Lang, S. Langish, H. Laqua, R. Laube, C. Lechte, M. Lennartz, W. Leonhardt, L. Lewerentz, Y. Liang, Ch. Linsmeier, S. Liu, J.-F. Lobsien, D. Loesser, J. Loizu Cisquella, J. Lore, A. Lorenz, M. Losert, L. Lubyako, A. Lcke, A. Lumsdaine, V. Lutsenko, J. Majano-Brown, O. Marchuk, M. Mardenfeld, P. Marek, S. Massidda, S. Masuzaki, D. Maurer, K. McCarthy, P. McNeely, A. Meier, D. Mellein, B. Mendelevitch, Ph. Mertens, D. Mikkelsen, O. Mishchenko, B. Missal, J. Mittelstaedt, T. Mizuuchi, A. Mollen, V. Moncada, T. Mnnich, T. Morizaki, R. Munk, S. Murakami, F. Musielok, G. Nfrdi, M. Nagel, D. Naujoks, H. Neilson, O. Neubauer, U. Neuner, T. Ngo, R. Nocentini, C. Nhrenberg, J. Nhrenberg, S. Obermayer, G. Offermanns, K. Ogawa, J. Ongena, J.W. Oosterbeek, G. Orozco, M. Otte, L. Pacios Rodriguez, W. Pan, N. Panadero, N. Panadero Alvarez, A. Panin, D. Papenfu, S. Paqay, A. Pavone, E. Pawelec, G. Pelka, X. Peng, V. Perseo, B. Peterson, A. Pieper, D. Pilopp, S. Pingel, F. Pisano, B. Plaum, G. Plunk, M. Povilaitis, J. Preinhaelter, J. Proll, M.-E. Puiatti, A. Puig Sitjes, F. Purps, M. Rack, S. Rcei, A. Reiman, D. Reiter, F. Remppel, S. Renard, R. Riedl, J. Riemann, S. Rimkevicius, K. Rie, A. Rodatos, H. Rhlinger, M. Rom, P. Rong, H.-J. Roscher, B. Roth, L. Rudischhauser, K. Rummel, T. Rummel, A. Runov, N. Rust, L. Ryc, S. Ryosuke, R. Sakamoto, A. Samartsev, M. Sanchez, F. Sano, S. Satake, G. Satheeswaran, J. Schacht, F. Schauer, T. Scherer, A. Schlaich, K.-H. Schlter, J. Schmitt, H. Schmitz, O. Schmitz, S. Schmuck, M. Schneider, W. Schneider, M. Scholz, P. Scholz, R. Schrittwieser, M. Schrder, T. Schrder, R. Schroeder, H. Schumacher, B. Schweer, B. Shanahan, I.V. Shikhovtsev, M. Sibilia, P. Sinha, S. Sipli, J. Skodzik, C. Slaby, H. Smith, W. Spiess, D.A. Spong, A. Spring, R. Stadler, B. Standley, L. Stephey, M. Stoneking, U. Stridde, Z. Sulek, C. Surko, Y. Suzuki, V. Szab, T. Szabolics, Z. Szkefalvi-Nagy, N. Tamura, A. Terra, J. Terry, J. Thomas, H. Thomsen, M. Thumm, C.P. von Thun, D. Timmermann, P. Titus, K. Toi, J.M. Travers, P. Traverso, J. Tretter, H. Tsuchiya, T. Tsujimura, S. Tulipn, M. Turnyanskiy, B. Unterberg, J. Urban, E. Urbonavicius, I. Vakulchyk, S. Valet, B. van Millingen, L. Vela, J.-L. Velasco, M. Vergote, M. Vervier, N. Vianello, H. Viebke, R. Vilbrandt, A. Vorkrper, S. Wadle, F. Wagner, E. Wang, N. Wang, F. Warmer, L. Wegener, J. Weggen, Y. Wei, J. Wendorf, A. Werner, B. Wiegel, F. Wilde, E. Winkler, V. Winters, S. Wolf, J. Wolowski, A. Wright, P. Xanthopoulos, H. Yamada, I. Yamada, R. Yasuhara, M. Yokoyama, J. Zajac, M. Zarnstorff, A. Zeitler, H. Zhang, J. Zhu, M. Zilker, A. Zimbal, A. Zocco, S. Zoletnik, and M. Zuin. Major results from the first plasma campaign of the Wendelstein 7-X stellarator. *Nuclear Fusion*, 57(10):102020, 2017.
- [44] E. Pasch, M. N. A. Beurskens, S. A. Bozhnikov, G. Fuchert, J. Knauer, R. C. Wolf, and W7-X Team. The Thomson scattering system at Wendelstein 7-X. *Review of Scientific Instruments*, 87:11E729, 2016.
- [45] A. Langenberg, N.A. Pablant, O. Marchuk, D. Zhang, J.A. Alonso, R. Burhenn, J. Svensson, P. Valson, D. Gates, M. Beurskens, R.C. Wolf, and the W7-X Team. Argon impurity transport studies at Wendelstein 7-X using x-ray imaging spectrometer measurements. *Nuclear Fusion*, 57(8):086013, 2017.
- [46] M. Yokoyama, H. Maaßberg, C.D. Beidler, V. Tribaldos, K. Ida, T. Estrada, F. Castejon, A. Fujisawa, T. Minami, T. Shimozuma, Y. Takeiri, A. Dinklage, S. Murakami, and H. Yamada. Core electron-root confinement (CERC) in helical plasmas. *Nuclear Fusion*, 47(9):1213, 2007.
- [47] C D Beidler, K Allmaier, M Yu Isaev, S V Kasilov, W Kernbichler, G O Leitold, H Maaßberg, D R

- Mikkelsen, S Murakami, M Schmidt, D A Spong, V Tribaldos, and A Wakasa. Benchmarking of the mono-energetic transport coefficients—results from the international collaboration on neoclassical transport in stellarators (icnts). *Nuclear Fusion*, 51:076001, 2011.
- [48] I. Calvo, J. L. Velasco, F. I. Parra, J. A. Alonso, and J. M. García-Regaña. Electrostatic potential variations on stellarator magnetic surfaces in low collisionality regimes. *J. Plasma Phys.* (accepted), 2018.
- [49] C. Brandt, T. Broszat, H. Thomsen, R. Laube, M. Marquardt, P. Franz, M. Schlke, T. Sieber, and S. Weiflog. Installation of the soft X-ray multi-camera tomography system (XMCTS) in the Wendelstein 7-X stellarator. *Fusion Engineering and Design*, 123:887 – 891, 2017. Proceedings of the 29th Symposium on Fusion Technology (SOFT-29) Prague, Czech Republic, September 5-9, 2016.
- [50] D. Zhang, R. Burhenn, R. Koenig, L. Giannone, P. A. Grodzki, B. Klein, K. Grosser, J. Baldzuhn, K. Ewert, V. Erckmann, M. Hirsch, H. P. Laqua, and J. W. Oosterbeek. Design criteria of the bolometer diagnostic for steady-state operation of the W7–X stellarator. *Review of Scientific Instruments*, 81(10):10E134, 2010.
- [51] J. A. Alonso, I. Calvo, J. M. García-Regaña, and J. L. Velasco. Can we use the variations of the electrostatic potential along flux surfaces to control impurity transport in stellarators? In *1st JPP Frontiers in Plasma Physics Conference*, 2017.